Water diffusion-transport in a synthetic dunite: Consequences for oceanic peridotite serpentinization

Benjamin Malvoisin [a,b,c,*], Fabrice Brunet [a]

[a] *ISTerre, Université de Grenoble I, CNRS, Maison des Géosciences, F-38041 Grenoble, France*
[b] *Laboratoire de Géologie, Ecole normale supérieure, CNRS, 24 rue Lhomond, 75231 Paris Cedex 5, France*
[c] *Institut des Sciences de la Terre, University of Lausanne, Géopolis, CH-1005 Lausanne, Switzerland*

A B S T R A C T

A series of San Carlos olivine aggregates, sintered at high pressure and high temperature, with two different porosities (around 1 and 10%) and grain sizes (1–5 μm and 0–38 μm) were reacted at 300 °C and 500 bars in the presence of pure water. The reaction progress was monitored magnetically and the composition and distribution of the reaction products were analyzed at the end of each experiment. Brucite formation mainly occurred at the aggregate surface as a result of both congruent olivine dissolution and aqueous Mg and Si buffering by the reaction products, i.e. brucite and lizardite. The measured reaction progress did not exceed 2.6% after 290 d, which strongly contrasts with previous studies performed on San Carlos olivine powders (i.e., isolated grains in aqueous solution). Hence, limited water transport through the intergranular region of the aggregate drastically decreased the olivine surface area accessible to water and thus slowed down the whole serpentinization process. When extrapolated to peridotite relevant olivine grain sizes, our experimental results indicate that the water diffusion rate will become so slow that the first layer of primary minerals exposed to water within a mesh structure must fully react before the next mineral layer starts reacting ("layer by layer" mechanism). This type of reaction-transport mechanism is obviously not consistent with the micro-scale serpentine distribution in the mesh of oceanic peridotite samples, therefore additional water transport pathways are required. Cracks formed under extensional thermal stresses are good candidates since, in comparison to grain boundary or reaction-induced fractures, they are wide enough to drastically enhance water transport in oceanic peridotites and therefore account for the observed textures. The 'layer by layer' mechanism inferred here can only set a lower time bound for serpentinization completion. Assuming a mesh size of 1 mm and an initial grain size of 100 μm and considering a temperature ranging from 100 to 300 °C with permanent water saturation, completion should take place within 100–1000 yr. Surprisingly, this duration represents only 1 to 10% of the estimated timescale of the natural serpentinization process, emphasizing the central role played by water availability in the natural reaction process.

© 2014 Elsevier B.V. All rights reserved.

1. Introduction

Hydrothermal circulation through upper-mantle rocks exhumed at slow-spreading ridges leads to the formation of serpentine minerals, $(Mg, Fe)_3Si_2O_5(OH)_4$ as the result of olivine and pyroxene hydration. The "serpentinization" reactions typically occur at temperatures below 450 °C and can produce, besides serpentine group minerals, variable amounts of magnetite, Fe_3O_4, brucite, $(Mg, Fe)(OH)_2$, and talc, $(Mg, Fe)_3Si_4O_{10}(OH)_2$.

The kinetics of the serpentinization process is expected to constrain a range of chemical and physical properties of the oceanic lithosphere: heat structure (Allen and Seyfried, 2004; Delescluse and Chamot-Rooke, 2008), hydrothermal circulation (Emmanuel and Berkowitz, 2006), hydrogen fluxes in slow-spreading centres (Charlou et al., 2002), deformation (Escartin et al., 1997) and magnetic signal build-up (Tivey and Dyment, 2010; Maffione et al., 2014).

For the sake of understanding its kinetics, serpentinization must be seen as a reaction-transport process which can be artificially decomposed into a sequence of steps: water is transported up to the peridotite minerals, typically olivine, $(Mg, Fe)_2SiO_4$, and orthopyroxene, $(Mg, Fe)_2Si_2O_6$ (step 1), which are then dissolved (step 2) and the produced aqueous species are transported (step 3)

Table 1
Experimental conditions and results.

Run	IGS (μm)	Duration (h)	S (%)	Porosity (%)	# Mg serp	# Mg bru	Polymorph	T_{RZ} (μm)	T_{RF} (μm)	NS
S1	0–38	1652	1.64	9 ± 2	0.96 ± 0.02	n.d.	Lizardite	44.6 ± 8.3	51.3 ± 15.3	121
S2	0–38	3434	1.32	0.7 ± 0.1	0.98 ± 0.01	0.95 ± 0.01	Lizardite	61.7 ± 11.6	41.0 ± 9.9	122
S3-1	1–5	1748	0.61	0.5 ± 0.1	0.98 ± 0.01	0.96 ± 0.01	Lizardite	20.8 ± 6.1	13.0 ± 5.3	125
S3-2	1–5	4104	1.12	0.5 ± 0.2	0.98 ± 0.01	0.96 ± 0.01	Lizardite	38.4 ± 9.1	16.5 ± 7.8	119
S3-3	1–5	6956	2.66	0.5 ± 0.3	0.99 ± 0.01	0.97 ± 0.01	Lizardite	48.8 ± 10.9	15.2 ± 6.2	88

Abbreviations are as follows: IGS, initial grain size; S, reaction progress; # Mg serp, Mg/(Mg + Fe) in serpentine; # Mg bru, Mg/(Mg + Fe) in brucite, Polymorph, serpentine polymorph; T_{RZ}, thickness of the reaction zone; T_{RF}, thickness of the reaction front; NS, number of sections across the sintered rim used for calculating the different parameters n.d.: not determined.

up to the locus of the reaction products precipitation (step 4). Each of these steps can potentially be rate limiting regarding the overall serpentinization process.

Serpentinization reactions have been widely studied experimentally in order to evaluate the respective role of temperature, pressure, grain size and starting composition on the chemistry and mineralogy of the reaction products and on their kinetics of formation (e.g., Martin and Fyfe, 1970; Moody, 1976; Wegner and Ernst, 1983; Seyfried et al., 2007; Marcaillou et al., 2011; Malvoisin et al., 2012b). In order to achieve significant extends of reaction at the laboratory timescale, these studies were quite exclusively performed using rock or mineral powders as starting material and, consequently, stages (1) and (3) were not investigated.

Extrapolation of serpentinization kinetic data derived from powder experiments predicts that grains of ∼100 μm, i.e., the typical grain size in peridotites, should react completely within tens of years. Consequently, serpentinization would represent an instantaneous process at the geological timescale (Malvoisin et al., 2012b). This inference is, however, not consistent with serpentinization reaction progresses estimated for abyssal peridotites, which are generally comprised between 40 and 100% (Oufi et al., 2002).

Consequently, water availability and/or species transport, i.e. step (1) and/or (3), are the likely rate limiting steps of the natural process and, the relevance of experimental studies performed on powders must therefore be questioned. Water involved in large scale hydrothermal circulation is mainly expected to flow (advection). Advection is an efficient process in oceanic lithosphere hydration as shown by the development of an hydrothermal circulation (Douville et al., 2002) which can only be reproduced numerically by using high peridotite permeability (10^{-14} to 10^{-13} m^2 Emmanuel and Berkowitz, 2006). Obviously, the high permeability of serpentinized peridotite is a consequence of rock fracturing which results from the combination (Rouméjon and Cannat, 2014) of deformation at mid-ocean ridges (McCaig et al., 2007; Hirose and Hayman, 2008), thermal cracking (Boudier et al., 2005; Demartin et al., 2013) and reaction-induced fracturing (Iyer et al., 2008; Jamtveit et al., 2008; Kelemen and Hirth, 2012; Plümper et al., 2012). However, the way serpentinization kinetics can be enhanced by fracturing remains controversial since volume increase associated to rock hydration should lead to pore clogging which will in turn decrease the rock permeability. The simulation of water advection in serpentinized peridotites is a complicated task since it will depend, in particular, on the geometry and the permeability of the fracture network. Numerical simulation (e.g., Emmanuel and Berkowitz, 2006; Iyer et al., 2012) is certainly the most appropriate mean to account for such complexity. At a smaller scale, microtextures of the serpentine veins in serpentinized peridotites suggest that advection occurs in the mesh network (cm scale and beyond) whereas hydration of the mesh cells (mm scale and below) is rather expected to operate through diffusion along mineral boundaries and microcracks, eventually through gel-like protoserpentine in the early serpentinization stages (Andreani et al., 2007; Boudier et al., 2010). In order to assess the respective part of reactivity and water diffusion (transport) on the kinetics of the serpentinization process, we followed an experimental approach; a synthetic dunite aggregates (sintered San-Carlos olivine) was reacted with pure water at 300 °C and 500 bars for various run durations. Reaction rates were compared to data collected with the same method, i.e., magnetic monitoring and analysis of scanning electron microscopy (SEM) images, under identical P–T conditions, on the same olivine material run as separate grains (powders) by Malvoisin et al. (2012b). Mass transfer of water/aqueous species during the serpentinization process was inferred from mineral phase distribution at the micrometer scale using again field emission-SEM data (FE-SEM data). The present set-up which involves as boundary condition the sample free surface in contact with water will prevent building up of significant deviatoric stress at the reaction interface. Processes such as reaction-induced fracturing which promote rock permeability will consequently not operate here.

2. Methods

Gem-quality San Carlos olivine (Fo$_{91}$) was finely crushed in an agate mortar and then calibrated at two initial grain sizes (IGS = 0–38 μm and 1–5 μm) with sieving and Stokes separation, respectively. Around 60 mg of calibrated powder were placed in a 3.5 mm diameter graphite sleeve and sintered in a piston–cylinder apparatus (see Brunet et al., 2003 for experimental set-up) at 1.5 GPa and 800 °C during 2 to 5 h to produce two cylinder aggregates of low porosity (ϕ), S1 and S3, with $\phi = 0.6 \pm 0.2\%$ (Table 1). An additional aggregate, S2, of higher porosity ($\phi = 9 \pm 2\%$) was prepared with the 0–38 μm powder in the same conditions but with a heating period limited to 10 min. Even if much of the deformation was accommodated by the protective graphite sleeve, decompression in the piston–cylinder apparatus at the end of the run led to disking of the sintered aggregate into 5 to 6 slices with a thickness between 1 and 2 mm. However, fracturing perpendicular to the slices was not observed. For each run, one of the slices was embedded in epoxy and polished parallel to its basal surface. Back-scattered electron images (BSE images) with a resolution of 0.28×0.28 μm^2 on a 1×1 mm area were acquired on the corresponding polished sections using the FE-SEM (Zeiss Sigma^{TM}, ENS, Paris). The surface area of both pores and olivine grains was computed by image analysis in order to retrieve a porosity estimate (Table 1). The remaining 4 to 5 slices were either loaded together (S1 and S2) or loaded separately as three different samples (S3) in Au-capsules (Malvoisin et al., 2013; 2 cm in length, 4.8 mm outer diameter and 4.4 mm inner diameter) together with deionized water (resistivity of 18 MΩ.cm) in a water to rock ratio of 2 for S1 and S2 and 4.5 for S3. Once welded shut, the capsules were placed in horizontal cold seal pressure vessels at a temperature of 300 °C $\pm$ 5 °C monitored with a Ni–NiCr thermocouple and regulated to within 1 °C (Brunet and Chopin, 1995). A pressure of 500 $\pm$ 50 bars was achieved by pumping argon into the vessel. Saturation remanent magnetization was also monitored *in-situ* with a cryogenic magnetometer (2G) available at ENS (Paris)

to retrieve the reaction rate following the procedure described in Malvoisin et al. (2012a). At the end of the experiment, reacted olivine aggregates were embedded in epoxy and polished parallel to their basal surface down to approximately half of their initial thickness. BSE images with a resolution of 0.28×0.28 μm^2 were then acquired on the polished sections ($\sim$3 mm in diameter) to characterize reaction products and microtextures, and to quantify the reaction progress by image analysis. The reaction products were analyzed under the FE-SEM with a 50 mm^2 energy dispersive spectrometry (EDS) detector (X-Max^{TM} from Oxford Instrument). Micro-Raman spectra (Renishaw InVia) were collected on the run products using a 514 nm incident laser beam (Renishaw InVia, ENS, and Horiba LabRAM HR, UNIL). To study the serpentinization kinetics, the reaction progress was inferred for each slice as follows. The volumetric production of reaction products was estimated by segmenting the BSE images into four distinct groups: magnetite, olivine, serpentine/brucite and epoxy. Serpentine and brucite could not be distinguished due to the small contrast difference between these two minerals on BSE images. Each pixel was assigned a group depending on its value compared to three fixed thresholds separating the four phase groups. These thresholds were determined for each image by plotting the BSE image histograms and finding the minimum between each phase group. Then, the volumetric proportions were converted into a measure of reaction progress using a thermodynamical model that explicitly takes the amount of secondary phases produced into account (see Malvoisin et al., 2012a, for details). The distribution of the reaction products across the sample was quantified in one dimension by dividing numerically the images in 88 to 125 rectangles with a dimension of 1400 by 60 μm regularly spaced perpendicular to the sample–water interface. The mineral proportions were estimated and first stacked along the longest side of each rectangle to obtain proportion profiles. These distribution profiles were stacked again to obtain a statistical distribution of the reaction products across the reaction zone. Fractures associated with the sample decompression after sintering in the piston–cylinder press were not considered in the image analysis. Two parameters were retrieved from image analysis: (1) the thickness of the reaction zone (T_{RZ}) which is defined as the zone containing more than 5 vol.% of reaction products and (2) the thickness of the reaction front (T_{RF}) which corresponds to the zone containing between 10 and 90 vol.% of San Carlos olivine (Table 1). T_{RZ} is directly related to the kinetics of water transport inwards the aggregate. T_{RF} is expected to increase when the ratio between water transport through the intergranular region (IGR, Brady, 1983) and serpentinization kinetics increases (as for powder samples).

Mineral compositions measured in our experiments were compared to calculated compositions using thermodynamical modeling in order to assess chemical equilibrium. For that purpose, we used the SUPCRT database (Johnson et al., 1992) to which the data for greenalite, $Fe_3Si_2O_5(OH)_4$, "ferroan brucite", $Fe(OH)_2$ and Fe^{3+} serpentine, $Fe_2Si_2O_5(OH)_4$ (Klein et al., 2009) were added; see Malvoisin et al. (2012a) for more details.

3. Results

3.1. Reaction products and microtextures

In all experiments, the olivine aggregate was surrounded by a thin reaction rim composed of serpentine, magnetite and brucite (Fig. 1a). Water penetration is monitored by the serpentine distribution. Both SEM images and Raman microspectrometry showed that serpentine only occurred at the rim of the aggregate in a zone comprised between the aggregate surface and the reaction front which separates the altered from the sound part of the aggregate. This zone will be called "reaction zone" in the following. Raman spectra acquired on serpentine in the high-frequency domain showed an intense peak at 3688 cm^{-1} and a secondary peak at 3703 cm^{-1} typical of lizardite (Auzende et al., 2004; Table 1). Even though small grains of magnetite ($\sim$1 μm across) were sparsely found in the reaction zone, magnetite mainly precipitated as euhedral to subhedral coarse grains (up to 30 μm in diameter) at the aggregate surface (Fig. 1b). In some instances, large magnetite is found to be made of an aggregation of smaller grains with individual sizes of $\sim$3 μm. Brucite which usually occurs as platelets was found as rectangular-shaped crystals in polished sections (10 to 100 μm length by 0.5 to 10 μm width) at the outermost part of the sample (Fig. 1a and c). Possibly, brucite did actually form platelets which crystallized parallel to the San Carlos aggregate surface and which are cut perpendicular in the sections. In the most reacted sample (S3-3), brucite was also found at the direct contact with olivine at a distance of 30 μm from the outer brucite rim (Fig. 1c). Mean Mg/(Mg+Fe) ratio in serpentine and brucite amounts to 0.98 ± 0.01 and 0.96 ± 0.01, respectively (Table 1), as determined using EDS under the FE-SEM.

3.2. Reaction front migration rate and reaction kinetics

The highest reaction progress (2.7%) was achieved in the was achieved in the S3-3 experiment which lasted 7000 h (Fig. 2b) whereas reaction progress of 80% was attained in only $\sim$1000 h with a San Carlos olivine powder of identical grain size and run in the same P–T conditions (Malvoisin et al., 2012b; Fig. 2a). Except for the first stage of the reaction ($<$400 h), called "zero stage" hereafter, where the serpentinization rate increased abruptly from, for example, $1.3 \times 10^{-4}\%$ h^{-1} to $1.2 \times 10^{-3}\%$ h^{-1} in S1, the reaction progress was found to vary linearly with time (Fig. 2b). In the narrow range of IGS investigated here, serpentinization kinetics was found to be IGS independent. Indeed, the two samples S2 and S3 with the same porosity ($\sim$0.6%) yielded comparable reaction rates although of different IGS (0–38 μm in S2 instead of 1–5 μm in S3). The serpentinization kinetics were found to depend on the aggregate porosity since reaction rates were three times higher in S1 ($1.2 \times 10^{-3}\%$ h^{-1}; porosity of $\sim$10%) compared to S2 ($4.0 \times 10^{-4}\%$ h^{-1}; porosity of 0.7%).

The thickness of the reaction zone (T_{RZ}) ranged from 20 to 60 μm (Figs. 3 and 4; Table 1) and increased, for each IGS, with time (Table 1; Fig. 4b). T_{RZ} was systematically higher for the 0–38 μm IGS than for the 1–5 μm ones (Fig. 4b) suggesting that, in the 0–38 μm aggregate, the olivine fraction with sizes below 1 μm reacted significantly faster and allowed for a deeper penetration of the reaction zone. Even though error bars on T_{RZ} are large, a significant dependence on porosity was also observed. Indeed, T_{RZ} increased 1.5 times faster in S1 than in S2 whereas the porosity was 10 times higher (Table 1). In order to investigate the rate of the reaction front migration, T_{RZ} was measured in S3, at three different reaction durations (1748 h, 4104 h and 6956 h). As illustrated on Fig. 3 and Fig. 4, the reaction zone widened and the density of the serpentine network increased with time. After an abrupt increase at the beginning of the reaction (zero stage, see above), T_{RZ} increased at a roughly constant rate of 0.0053 μm/h $\pm$ 0.0032 μm/h.

The thickness of the reaction front (T_{RF}) was found to depend on the IGS with T_{RF} approximately equals to three times the IGS ($T_{RF} = 46 \pm 17$ μm and 14.9 ± 8 μm for IGS of 0–38 μm and 1–5 μm, respectively).
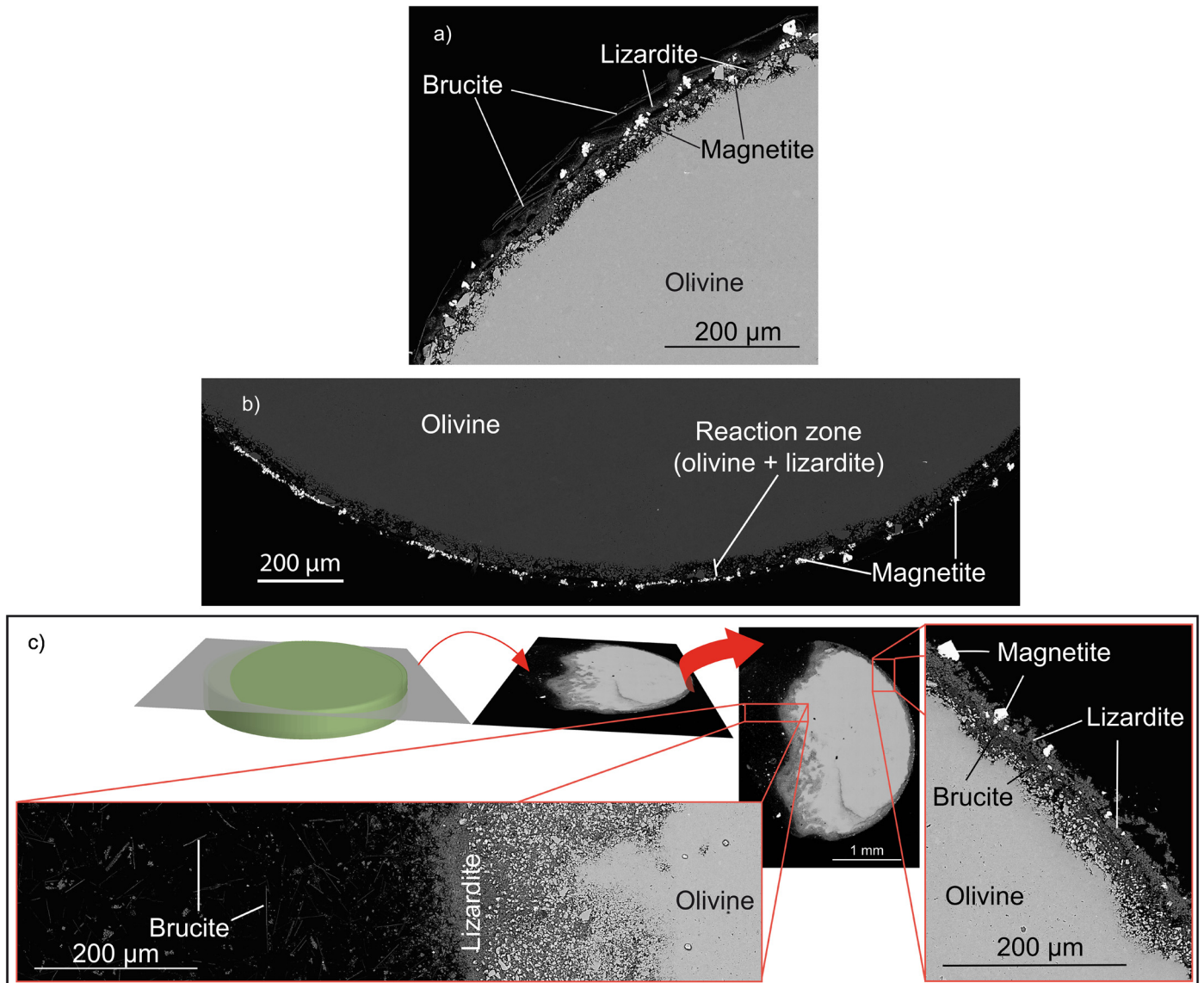
Fig. 1. BSE images of the reaction rim along sections perpendicular (a and b) or oblique (c) to the basal surface of reacted aggregate cylinder. (a and b). Sections across S2 showing the precipitation at the rim of the aggregate of platy brucite and aligned magnetite grains. (b) Higher contrast image. (c) Sketch of the position of the section across S3-3, full section and enlargements showing the formation of platy brucite at the aggregate rim (left) or at the contact with olivine (right).
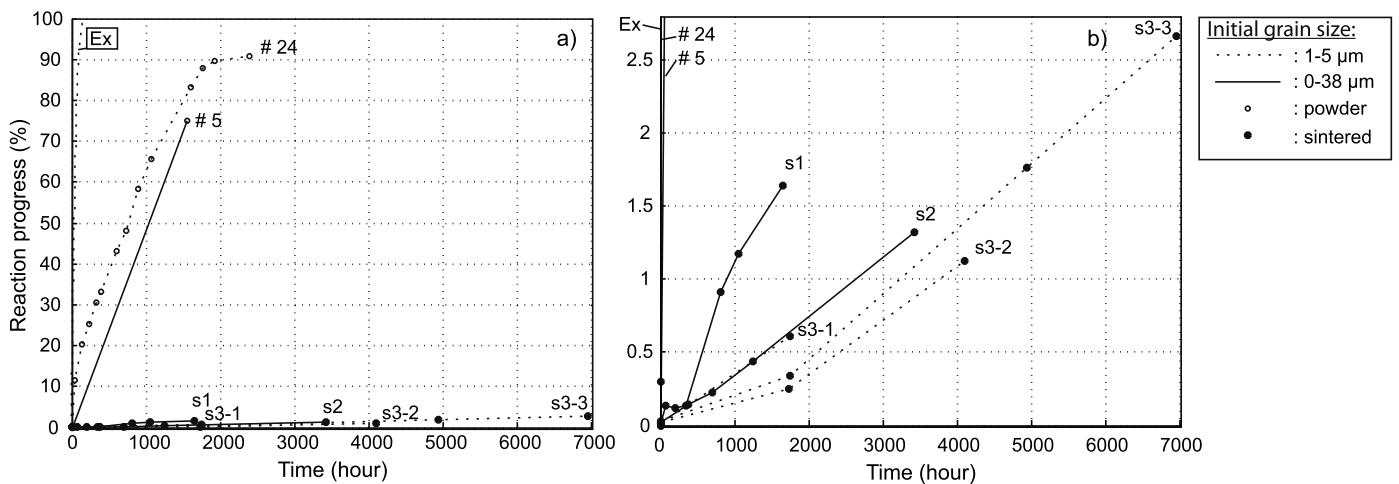

Fig. 2. Kinetic data derived from magnetic monitoring of olivine serpentinization. (a) Comparison with experiments on powders (either measured: runs 5 and 24, or extrapolated: Ex) and on sintered (runs S1, S2, S3-1, S3-2 and S3-3). Note the orders of magnitude of difference in reaction rates for comparable IGS. (b) Limited reaction progress for the experiments on the olivine aggregate. The higher reaction rate for S1 is associated with a porosity ∼10 times higher than in the other experiments.
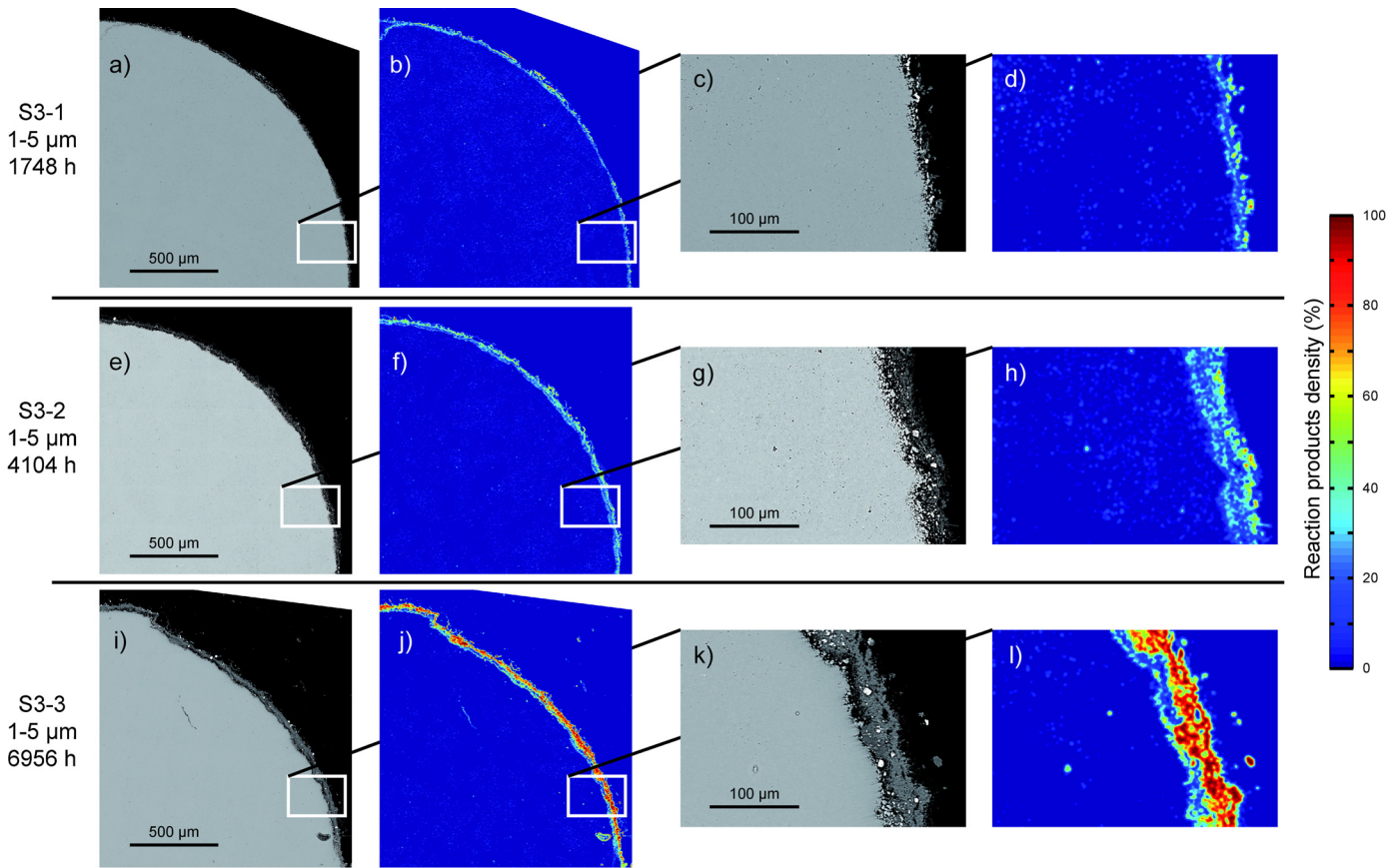
Fig. 3. BSE images and corresponding reaction products density maps for sections perpendicular to the basal surface of the aggregate cylinder having the same porosity ($\phi \sim 1\%$) and the same IGS (1–5 μm), but reacted for different duration (1748 h in a to d, 4104 h in e to h, and 6956 h in i to l). (c, d), (g, h) and (k, l) are enlargements of the zones depicted with white squares on (a, b), (e, f) and (i, j), respectively. The reaction products density is the ratio of pixels identified as being associated with lizardite, brucite or magnetite over the total amount of pixels in a 20×20 pixels box. Note the increase in reaction zone width and the decrease of its porosity as a function of time.
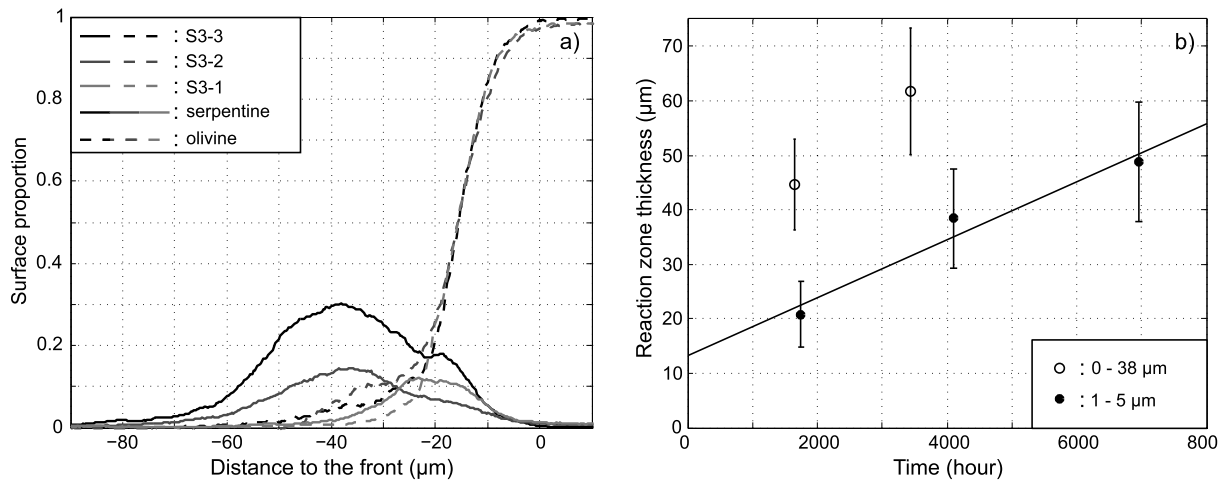

Fig. 4. (a) Surface proportion of olivine and serpentine across the rim of samples S3-1, S3-2 and S3-3 having the same porosity ($\phi \sim 1\%$) and the same IGS (1–5 μm), but different run durations (1748 h, 4104 h and 6956 h, respectively). Note the constant geometry of the reaction front and the progressive widening of the reaction zone as a function of time. (b) Reaction zone thickness (T_{RZ}) as a function of time for all the experiments. The reaction zone thickness is defined as the zone where more than 5 vol.% of reaction products is observed. Note the proportionality between the T_{RZ} and the time for S3-1, S3-2 and S3-3. The rapid growth of the T_{RZ} at the beginning of the reaction is interpreted as resulting from the "zero stage".

4. Discussion

4.1. Water transport versus reaction kinetics

Compared to powder experiments, the nature of the serpentine polymorph differs since lizardite is produced here whereas chrysotile was formed from olivine powders of IGS < 5 μm, hy-drated at 300 °C and 500 bars (Malvoisin et al., 2012b). This result is consistent with the comparatively low serpentinization kinetics obtained here for sintered aggregates as compared to powders of same grain sizes. However, the rate limiting step (i.e., olivine dissolution or serpentine mineral precipitation) cannot be inferred from the present experimental dataset, it can, at best, be bracketed using the kinetics dataset derived on San Carlos olivine pow-

ders (Malvoisin et al., 2012b). At the olivine grain size used here (1–5 μm), chrysotile formed in the powder experiments and, the formation of the mineral products was interpreted as the rate-limiting step of the serpentinization reaction. For larger grain sizes, lizardite crystallized and San Carlos olivine dissolution was shown to be the rate limiting step. Extrapolated down to the 1–5 μm grain size range, this latter kinetics is obviously the highest. We considered here that olivine serpentinization within a reacting layer of the aggregate must proceed at a rate comprised between the two latter kinetics, i.e., with chrysotile precipitation as the rate limiting step on the one hand, and with olivine dissolution as the rate limiting step on the other hand (Malvoisin et al., 2012b; Fig. 2): The difference between these two being around one order of magnitude.

Based on observations of S1 aggregate prior to reaction, the "zero" stage is interpreted as an artefact resulting from the high dissolution rate of the first micrometers of the olivine aggregate. This high rate likely results from sintering which produced a rough aggregate surface with a large reactive surface area. Without taking into account this "zero stage" in the calculation, rates of olivine serpentinization reported here are two to three orders of magnitude slower than those measured in the same conditions (IGS, pressure and temperature) on powders ($\sim 4 \times 10^{-4}$% h^{-1} for SC olivine aggregate to be compared to 4×10^{-2} to 5×10^{-1}% h^{-1} for SC olivine powder; Fig. 2; Malvoisin et al., 2012b). This difference can be accounted for by the large proportion of grain surface in the aggregate which is not available to water. The available surface area is thus about two orders of magnitude smaller than for the powder of equivalent IGS.

The reaction zone is limited by a reaction front which propagates inwards at a roughly constant rate. Reaction products are not observed in the interior of the aggregate indicating a low permeability due to limited connections between pores. The reaction front which is outlined by the appearance of lizardite can be assumed to reflect the water propagation front in the aggregate. At the scale of the reacted zone, the propagation rate of the reaction front (v_{rf}) is therefore not affected by a limitation in water availability due for example to clogging of porosity by the reaction products. This is in line with the high porosity of the serpentine network observed on SEM images (Fig. 1). Values of v_{rf} obtained here ($v_{rf} \sim 0.005$ μm/h in S3; IGS = 1–5 μm and $\phi \sim 0.6$%) are by 20 times higher than the equivalent rate estimated for a single olivine grain having the same volume ($v_\infty \sim 2.5 \times 10^{-4}$ μm/h; Malvoisin et al., 2012b). This clearly demonstrates that the aggregate cannot be considered as a single grain owing to the presence between olivine grains of an IGR composed of grains boundaries and pores which act as preferential path for water diffusion. In sintered olivine, grain boundaries typically display widths of ~ 1 nm (e.g., Faul and Gerald, 1999; Hiraga and Kohlstedt, 2007). Due to the relatively low temperature and short sintering duration applied here, pores remain and therefore olivine grain boundaries are not continuous. The reaction front is not sharp but composed of a zone where olivine grains are isolated in a lizardite medium. Due to the highly porous nature of this lizardite medium, surfaces are accessible to water and olivine grains behave as in a powder. Assuming that water supply is not limiting, the serpentinization kinetics determined on San Carlos olivine powders by Malvoisin et al. (2012b) should then apply to this reaction front (Fig. 5b, f and g). For the sake of simplicity, we used in the following a first-order reaction kinetics with a rate constant k depending on the IGS instead of the Avrami's law proposed in Malvoisin et al. (2012b). This simplification has negligible effect on the modeling of reaction front propagation compared to the uncertainty on the other input parameters such as T_{RF}. As the serpentine network in the reaction zone is highly porous, the water concentration (C), used in the following to describe the reaction

front, is considered to be equal to 1 where the olivine is completely reacted and to 0 where olivine has not reacted. The two processes occurring at the reaction front are olivine hydration and water diffusion in the IGR which impact the water concentration as follows:

$$\frac{\partial C}{\partial t} = D_{eff} \frac{\partial^2 C}{\partial x^2} - kC \qquad (1)$$

with D_{eff} the effective diffusion coefficient of water in the olivine aggregate. As the reaction front propagates at a constant rate, v_{rf}, the system is at steady state in the referential of the reaction front for which $x = v_{rf}/t$ with t, the time. By analogy with the definition of T_{RF}, the water concentration at the reaction front ($x = 0$) can be fixed to $C = 0.9$ and, since water does not permeate up to the center of the aggregate, $C \to 0$ when $x \to \infty$. Using these boundary conditions, the solution of Eq. (1) at steady state ($\frac{\partial C}{\partial t} = 0$) is:

$$C = 0.9 \exp\left(-x\sqrt{k/D_{eff}}\right) \qquad (2)$$

As $C = 0.1$ in $x = T_{RF}$, this equation allows to retrieve the effective diffusion coefficient from k and T_{RF}:

$$D_{eff} = \frac{kT_{rf}^2}{(\ln(9))^2} \qquad (3)$$

For S3 with values of k and T_{RF} comprised between 4.0×10^{-7} and 5.0×10^{-6} s^{-1} and 14.9 ± 8 μm, respectively, D_{eff} is comprised between 4.0×10^{-18} and 5.4×10^{-16} m^2 s^{-1}.

The diffusivity in the IGR largely exceeds intracrystalline diffusivity in olivine at the temperature of the experiments which can therefore be neglected. Assuming a 3D cubic array of mantled mineral cubes with diffusion paths perpendicular to the cube faces, then $D_{eff} \propto D_{IGR} \frac{\delta}{IGS}$ where δ is the IGR thickness (Fig. 5b and c). Considering that δ does not vary with grain size, D_{eff} can be extrapolated to any IGS. The corresponding dependence of D_{eff} on the IGS can be combined to the dependence of k on the IGS derived from Malvoisin et al. (2012b) to estimate, from Eq. (3), the dependence of T_{RF} on the IGS. The T_{rf}/IGS ratio drops to become lower than 0.5 for IGS > 20 μm. This suggests that, in a natural peridotite having a typical IGS of 100 μm, the kinetics of reaction will be mainly controlled by olivine reaction rate rather than by water penetration. Obviously, this conclusion holds only if D_{eff} value determined here still applies at larger IGS; this is unlikely since other processes such as fracturing can potentially increase D_{eff} (Rudge et al., 2010), see Section 4.3.

4.2. Transport-chemistry coupling and brucite segregation

In all the experiments, the olivine aggregate–water interaction produced a reaction zone with a mineral zoning from relatively pure lizardite at the interface with unreacted olivine to a rim of subhedral magnetite grains followed by an outermost rim of brucite (see Fig. 1). As regarding serpentine and magnetite, this type of mineral segregation recalls the typical mesh textures described in natural serpentinized peridotites, in which olivine is surrounded by a rim of serpentine, itself outlined by coarse magnetite grains (Wicks and Whittaker, 1977; Oufi et al., 2002). However, the segregation of brucite observed here at tens of micrometers from the dissolving olivine has never been described before in experimental studies. In the case of the most reacted sample (S3-3 with a reaction rim of ~ 50 μm), brucite was also found to precipitate at the contact with dissolving olivine, in the innermost part of the reaction zone, suggesting that a second brucite segregation zone is forming in this sample. In serpentinized dunites, brucite can be found away from olivine grains in the core of serpentinite veins (Plümper et al., 2012; Frost et al., 2013) or directly precipitated onto the olivine surface (Klein et al., 2009;
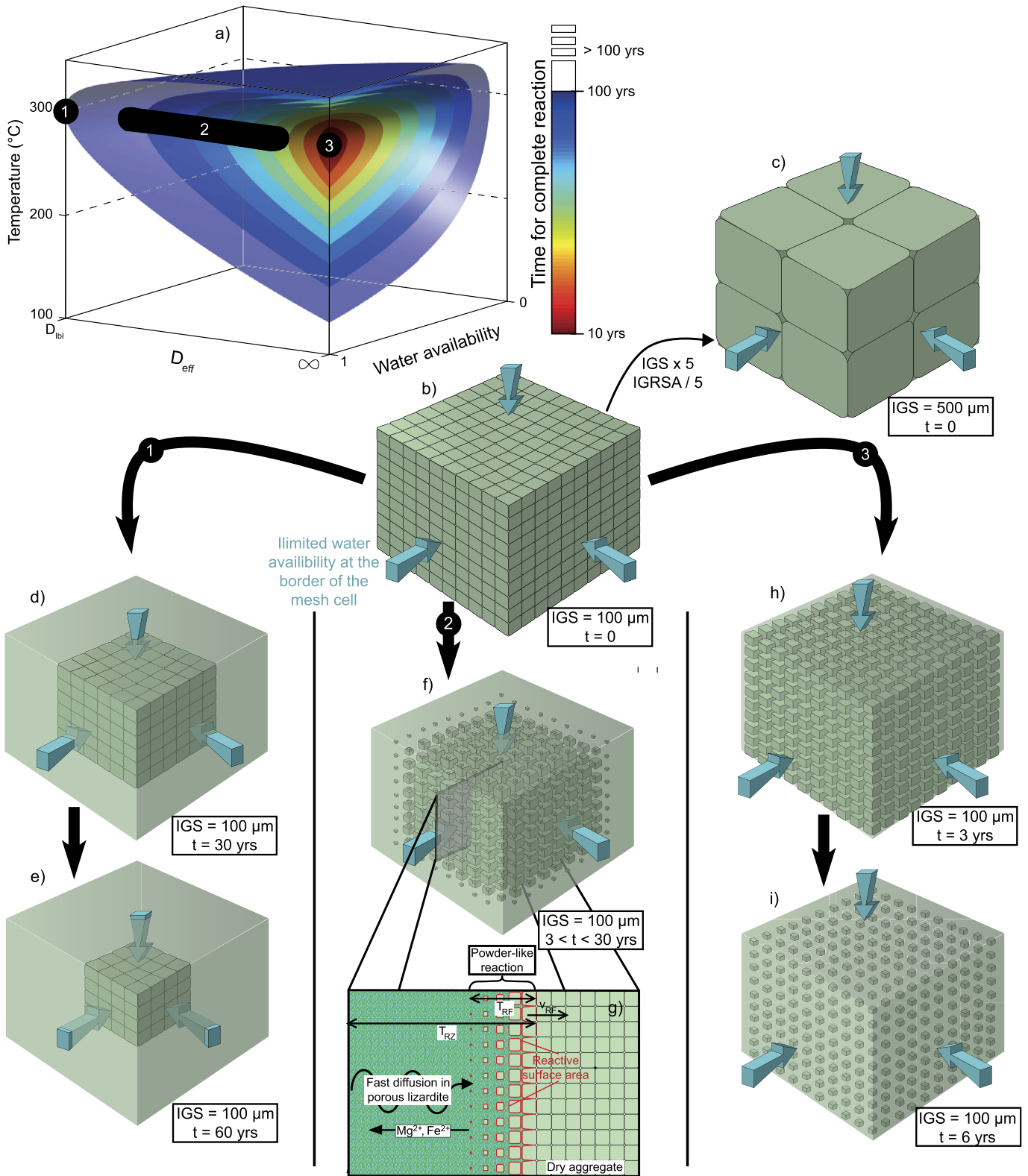
Fig. 5. Reaction time and mechanisms for the serpentinization of an olivine aggregate within a 1 mm mesh size and a grain size of 100 μm. (a) Hypothetical diagram of the dependence on temperature, water diffusivity (D_{eff}) and water availability of the time for a complete reaction of the aggregate. The water availability is fixed to 0 when water is absent and to 1 when the system is saturated. D_{eff} has for lower bound the water diffusivity measured in our experiments (D_{lbl}) and tends towards infinite values when the aggregate reacts as a powder. Because the relationships between D_{eff}, water availability and the time for reaction completion are not known, linear relationships are arbitrarily used here. The dependence of the reaction completion time on temperature determined on powders by Malvoisin et al. (2012b) was used here. Point 1 and associated sketches (b, d and e) represent an extrapolation of the data acquired in the present study with the "layer by layer" mechanism. Point 2, associated sketches (b and f) and cross-section (g) correspond to a mechanism where the diffusion coefficient is intermediate between D_{lbl} and ∞. The resulting reaction mechanism corresponds to coupled reaction–diffusion where grains are progressively isolated from the aggregate and react as in a powder sample. This mechanism accounts for our observation for the small IGS of our experiments. Point 3 and associated sketches (b, h and i) correspond to the case where water diffusivity is ∞ and where the whole aggregate behaves as a powder. The comparison between (b) and (c) illustrates the dependence of IGR surface area (*IGRSA*) on IGS.
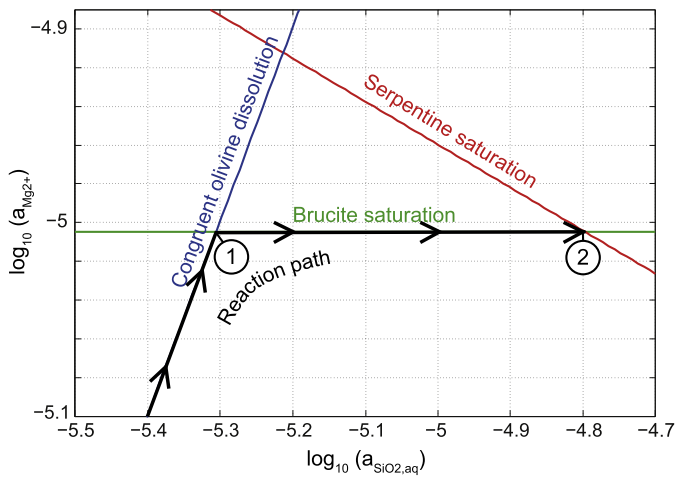
Fig. 6. $a_{Mg^{2+}}$–$a_{SiO_2,aq}$ diagram of the evolution of the fluid composition assuming congruent olivine dissolution ($a_{Mg^{2+}}/a_{SiO_2,aq} = 2$). The fluid composition first reaches the brucite saturation curve (Point 1). Then, brucite precipitates alone from Point 1 to Point 2 until the fluid composition reaches the intersection between brucite and serpentine saturation curves. At this point, the two minerals precipitate together and the fluid composition is fixed. To construct this diagram, mineral saturation was computed with SUPCRT92 (Johnson et al., 1992).

Ogasawara et al., 2013). These two types of occurrences can be accounted for by the same sequential process of magnesium transport followed by brucite precipitation at energetically favourable sites; the main difference between these occurrences being the transport distance of aqueous magnesium. Brucite segregation associated with magnesium transport has clearly been observed in powder experiments (Malvoisin et al., 2012b; Supplementary Fig. S1).

We modeled the reaction path followed by the aqueous solution at the early stages of the experiment, i.e. before reaching steady-state conditions at which the fluid composition becomes buffered by the reaction products. For the sake of simplicity, aqueous silica and magnesium were considered as the only aqueous species so that pH and Mg^{2+} activity are directly related to each other ($a_{Mg^{2+}} = a_{OH^-}/2$). Furthermore, congruent olivine dissolution was assumed implying $[Mg^{2+}]/[SiO_2,aq] = 2$ and infinite kinetics were considered for mineral precipitation (i.e., no supersaturation). It can be seen in an activity–activity diagram (Fig. 6) that the fluid composition first reaches the brucite saturation curve. Then, as olivine dissolution proceeds further, brucite keeps precipitating while aqueous silica activity increases in the solution until it reaches serpentine saturation. At this point, the fluid composition is buffered by the brucite + serpentine assemblage so that the activity of Mg^{2+} and SiO_2,aq is fixed. According to this model, at 300 °C and 500 bars, 2 nmoles of brucite should precipitate at the sample surface until the serpentinite saturation is reached, i.e. reaction progress of 10^{-3}%. At larger reaction progresses, i.e. after steady fluid composition is reached (Point 2 in Fig. 6), brucite remains only located at the surface of the samples, in the form of large euhedral grains (Fig. 1). It can be inferred that brucite did no longer nucleate and, instead, in order to minimize surface energy, the formation of additional brucite was accounted for by grain coarsening from the brucite seeds which formed before Point 2 had been attained by the solution (Fig. 6). Sample S3-3 suggests that at some stage, when the diffusion distance between dissolving olivine and growing brucite becomes too large, brucite supersaturation is achieved in the vicinity of dissolving olivine and a second zone with new brucite seeds may form.

Due to the higher reactivity of olivine in comparison to pyroxene, the early formation of brucite at the aggregate–fluid interface as evidenced experimentally here is also to be ex-

pected in pyroxene-bearing rocks. Transposing our experimental data to a peridotite system, brucite would be expected to preferentially crystallize (and grow) in the zones of fresh fluid (serpentine-undersaturated) circulation, possibly within the mesh network. Conversely, due to their location, brucite grains if any, will be preferentially exposed to dissolution or reaction with aqueous silica dissolved in the circulating fluids to form serpentine.

4.3. Serpentinization kinetics: what do we learn from laboratory experiments?

A summary of the mechanisms of serpentinization discussed hereafter can be found in Fig. 5. This figure outlines the parameters controlling the occurrence of the different mechanisms.

When a synthetic dunite aggregate is reacted at 300 °C and 500 bars with pure water, we showed that the serpentinization kinetics are two to three orders of magnitude slower than with powders of the same material with identical grain sizes. The difference between these two types of experiments allows to probe the effect of mass transfer (primarily water) on the kinetics of the serpentinization process. Serpentinization kinetics have been modeled, for the very small reaction progresses achieved in our experiments, by using a reaction–diffusion model which leads to the formation of a reaction zone where olivine grain hydration kinetics are comparable to that of a powder and where water is permanently available. Extrapolation of the diffusion coefficient calculated for S3 with this simple model reveals that the reaction front thickness becomes twice as small as the IGS itself for IGS > 20 μm. The first row of grains must react before the second one starts to be affected and a sharp hydration front is expected to develop (Fig. 5b, d, and e). With this 'layer by layer' mechanism, the overall reaction rate will be controlled by the olivine dissolution kinetics which depends on the composition of the solution and on water supply; constantly renewed seawater circulating in the rock will maintain far-from equilibrium conditions and lead to faster reaction than static conditions

The microtexture resulting from a 'layer-by-layer' mechanism with a sharp front separating fully reacted olivine from unreacted one is definitely not observed in serpentinized peridotites where most olivine grains are surrounded and cross-cut by serpentine (e.g. Rumori et al., 2004). The water transport through natural peridotites must thus be significantly higher than derived here (Fig. 5a, h and i) on the only basis of water diffusion through the intergranular medium of a sintered olivine aggregate. While the porosity of oceanic peridotites is not expected to differ significantly from the smallest porosity used here, permeability is expected to be larger mainly due to the presence of microcracks (MacDonald and Fyfe, 1985). Higher permeability coupled to the circulation of a constantly renewed solution might be the reason why the rate of serpentinization obtained in the percolation experiments of Godard et al. (2013) on an aggregate of SC olivine with a porosity of 12% and an IGS of 150–300 μm was, respectively, ∼30 and ∼100 times faster than the rates measured here, in a close system, on SC olivine within an aggregate with a porosity of 10% and an IGS of 1–5 μm (S1) or with powders with IGS of 100–150 μm (Malvoisin et al., 2012b).

The development of a connected network of cracks with apertures exceeding that of olivine grain boundary appears as a way to enhance water transport within oceanic peridotite bodies either by diffusion or advection. In natural settings, the combination of extensional stress and thermal contraction respectively associated with regional tectonics and peridotite cooling, is the likely candidate for the development of crack networks (Rouméjon and Cannat, 2014). For example, Boudier et al. (2010) determined that cracks with a maximum width of ∼1 μm, i.e. three orders of

magnitude higher than typical grain boundary width, should form around grains with sizes of 200 μm during peridotite cooling from 800 °C to 400 °C. Our results suggest that, in comparison, the formation of mesh textures on the only basis of microcracks developed by reaction-induced fracturing will be difficult. Indeed, such microcracks have a typical width at their tip of ∼5 nm (Plümper et al., 2012) which is basically close to grain boundary widths (∼1 nm, Hiraga and Kohlstedt, 2007). Even if the influence on water transport of the widening of these cracks by deformation associated with reaction-induced pressure increase has still to be investigated, water transport in these cracks is expected to proceed at rates similar to the one observed in our experiments.

Serpentinization kinetics at the mesh scale deduced from the extrapolation of our laboratory data must be considered as a lower bound. In water saturated conditions, i.e. when water saturated conditions are permanently achieved around the grains, the time required for the complete reaction of a single grain of 100 μm is on the order of 10 yr at 300 °C and 100 yr at 100 °C (Malvoisin et al., 2012b). For a serpentinized peridotite in which ∼1 mm width mesh cells are formed, the corresponding minimum characteristic time for serpentinization completion is thus of 100 yr at 300 °C and 1000 yr at 100 °C assuming permanent excess of aqueous solution with a composition which is buffered by the brucite–lizardite assemblage (Fig. 5a, b and d). The estimated duration of hydrothermal activity at an hydrothermal field located on an ultramafic substratum such as Lost City is of 30,000 yr (Früh-Green et al., 2003), that is one to two orders of magnitude longer than the timescale determined here. Therefore, peridotites recovered at mid-ocean ridges should be fully serpentinized what is not the case (Oufi et al., 2002). This discrepancy is likely related to the fact that we assumed permanent water saturation whereas water supply might be discontinuous depending on the hydrodynamics of mid-ocean ridges hydrothermal systems which appear to evolve with time at least at the local scale of hydrothermal fields (Barreyre et al., 2012; Rouméjon and Cannat, 2014). Assuming complete serpentinization at water saturated conditions in 100–1000 yr and a time scale of serpentinization of 10,000 yr, we can infer that the time fraction during which water is effectively available for serpentinization to proceed (water sporadicity factor) is around 0.01–0.1.

Acknowledgements

Appendix A. Supplementary material

Supplementary material related to this article can be found online at http://dx.doi.org/10.1016/j.epsl.2014.07.004.

References

Andreani, M., Mével, C., Boullier, A.-M., Escartin, J., 2007. Dynamic control on serpentine crystallization in veins: constraints on hydration processes in oceanic peridotites. Geochem. Geophys. Geosyst. 8, 1–24.

Allen, D.E., Seyfried, W.E., 2004. Serpentinization and heat generation: constraints from Lost City and Rainbow hydrothermal systems. Geochim. Cosmochim. Acta 68, 1347–1354.

Auzende, A.L., Daniel, I., Reynard, B., Lemaire, C., Guyot, F., 2004. High-pressure behaviour of serpentine minerals: a Raman spectroscopic study. Phys. Chem. Miner. 31, 269–277.

Barreyre, T., Escartin, J., Garcia, R., Cannat, M., Mittelstaedt, E., Prados, R., 2012. Structure, temporal evolution, and heat fluxes estimates from the Lucky Strike deep-sea hydrothermal field derived from seafloor image mosaics. Geochem. Geophys. Geosyst. 13, 1–29.

Boudier, F., Nicolas, A., Mainprice, D., 2005. Does anisotropy of thermal contraction control hydrothermal circulation at Moho level below fast spreading oceanic ridges? Int. Geol. Rev. 47, 101–112.

Boudier, F., Baronnet, A., Mainprice, D., 2010. Serpentine mineral replacements of natural olivine and their seismic implications: oceanic lizardite versus subduction-related antigorite. J. Petrol. 51, 495–512.

Brady, J.B., 1983. Intergranular diffusion in metamorphic rocks. Am. J. Sci. 283-A, 181–200.

Brunet, F., Chopin, C., 1995. Bearthite, Ca$_2$Al(PO$_4$)$_2$OH – stability, thermodynamic properties and phase-relations. Contrib. Mineral. Petrol. 121, 258–266.

Brunet, F., Bagdassarov, N., Miletich, R., 2003. Na$_3$Al$_2$(PO$_4$)$_3$, a fast sodium conductor at high pressure: in-situ impedance spectroscopy characterisation and phase diagram up to 8 GPa. Solid State Ion. 159, 35–47.

Charlou, J.L., Donval, J.P., Fouquet, Y., Jean-Baptiste, P., Holm, N., 2002. Geochemistry of high H$_2$ and CH$_4$ vent fluids issuing from ultramafic rocks at the Rainbow hydrothermal field (36°14′N, MAR). Chem. Geol. 191, 345–359.

Delescluse, M., Chamot-Rooke, N., 2008. Serpentinization pulse in the actively deforming Central Indian Basin. Earth Planet. Sci. Lett. 276, 140–151.

Demartin, B., Hirth, G., Evans, B., 2013. Experimental constraints on thermal cracking of peridotite at oceanic spreading centers. In: Geophysical Monograph Series, vol. 148.

Douville, E., Charlou, J.L., Oelkers, E.H., Bienvenu, P., Jove Colon, C.F., Donval, J.-P., Fouquet, Y., Prieur, D., Appriou, P., 2002. The rainbow vent fluids (36°14′N, MAR): the influence of ultramafic rocks and phase separation on trace metal content in Mid-Atlantic Ridge hydrothermal fluids. Chem. Geol. 184, 37–48.

Emmanuel, S., Berkowitz, B., 2006. Suppression and stimulation of seafloor hydrothermal convection by exothermic mineral hydration. Earth Planet. Sci. Lett. 243, 657–668.

Escartin, J., Hirth, G., Evans, B., 1997. Effects of serpentinization on the lithospheric strength and the style of normal faulting at slow-spreading ridges. Earth Planet. Sci. Lett. 151, 181–189.

Faul, U.H., Gerald, J.D.F., 1999. Grain misorientations in partially molten olivine aggregates: an electron backscatter diffraction study. Phys. Chem. Miner. 26, 187–197.

Frost, B.R., Evans, K.A., Swapp, S.M., Beard, J.S., Mothersole, F.E., 2013. The process of serpentinization in dunite from New Caledonia. Lithos 178, 24–39.

Früh-Green, G.L., Kelley, D.S., Bernasconi, S.M., Karson, J.A., Ludwig, K.A., Butterfield, D.A., Boschi, C., Proskurowski, G., 2003. 30,000 years of hydrothermal activity at the Lost City vent field. Science 301, 495–498.

Godard, M., Luquot, L., Andreani, M., Gouze, P., 2013. Incipient hydration of mantle lithosphere at ridges: a reactive-percolation experiment. Earth Planet. Sci. Lett. 371–372, 92–102.

Hiraga, T., Kohlstedt, D.L., 2007. Equilibrium interface segregation in the diopside–forsterite system I: analytical techniques, thermodynamics, and segregation characteristics. Geochim. Cosmochim. Acta 71, 1266–1280.

Hirose, T., Hayman, N.W., 2008. Structure, permeability, and strength of a fault zone in the footwall of an oceanic core complex, the Central Dome of the Atlantis Massif, Mid-Atlantic Ridge, 30°N. J. Struct. Geol. 30, 1060–1071.

Iyer, K., Jamtveit, B., Mathiesen, J., Malthe-Sørensen, A., Feder, J., 2008. Reaction-assisted hierarchical fracturing during serpentinization. Earth Planet. Sci. Lett. 267, 503–516.

Iyer, K., Rüpke, L.H., Morgan, J.P., Grevemeyer, I., 2012. Controls of faulting and reaction kinetics on serpentinization and double Benioff zones. Geochem. Geophys. Geosyst. 13.

Jamtveit, B., Malthe-Sorensen, A., Kostenko, O., 2008. Reaction enhanced permeability during retrogressive metamorphism. Earth Planet. Sci. Lett. 267, 620–627.

Johnson, J.W., Oelkers, E.H., Helgeson, H.C., 1992. SUPCRT92: a software package for calculating the standard molal thermodynamic properties of minerals, gases, aqueous species, and reactions from 1 to 5000 bar and 0 to 1000. Comput. Geosci. 18, 899–947.

Kelemen, P.B., Hirth, G., 2012. Reaction-driven cracking during retrograde metamorphism: olivine hydration and carbonation. Earth Planet. Sci. Lett. 345–348, 81–89.

Klein, F., Bach, W., Jöns, N., McCollom, T., Moskowitz, B., Berquo, T., 2009. Iron partitioning and hydrogen generation during serpentinization of abyssal peridotites from 15°N on the Mid-Atlantic Ridge. Geochim. Cosmochim. Acta 73, 6868–6893.

Macdonald, A.H., Fyfe, W.S., 1985. Rate of serpentinization in seafloor environments. Tectonophysics 116, 123–135.

Maffione, M., Morris, A., Plümper, O., van Hinsbergen, D.J.J., 2014. Magnetic properties of variably serpentinized peridotites and their implication for the evolution of oceanic core complexes. Geochem. Geophys. Geosyst. 15, 923–944.

Malvoisin, B., Carlut, C., Brunet, F., 2012a. Serpentinization of oceanic peridotites. 1. A high-sensitivity method to monitor magnetite production in hydrothermal experiments. J. Geophys. Res. 117.

Malvoisin, B., Brunet, F., Carlut, J., Rouméjon, S., Cannat, M., 2012b. Serpentinization of oceanic peridotites. 2. Kinetics and processes of San Carlos olivine hydrothermal alteration. J. Geophys. Res. 117.

Malvoisin, B., Brunet, F., Carlut, J., Montes-Hernandez, G., Findling, N., Lanson, M., Vidal, O., Bottero, J.-Y., Goffé, B., 2013. High-purity hydrogen gas from the reac-

tion between BOF steel slag and water in the 473–673 K range. Int. J. Hydrog. Energy 38 (7382), 7393.

Marcaillou, C., Munerg, M., Vidal, O., Parra, T., Harfouche, M., 2011. Mineralogical evidence for H_2 degassing during serpentinization at 300 gas from t. Earth Planet. Sci. Lett. 303, 281–290.

Martin, B., Fyfe, W.S., 1970. Some experimental and theoretical observations on the kinetics of hydration reactions with particular reference to serpentinization. Chem. Geol. 6, 185–202.

Moody, J.B., 1976. An experimental study on the serpentinization of iron-bearing olivines. Can. Mineral. 14, 462–478.

McCaig, A.M., Cliff, R.A., Escartin, J., Fallick, A.E., MacLeaod, C.J., 2007. Oceanic detachment faults focus very large volumes of black smokers fluids. Geology 35, 935–938.

Ogasawara, Y., Okamoto, A., Hirano, N., Tsuchiya, N., 2013. Coupled reactions and silica diffusion during serpentinization. Geochim. Cosmochim. Acta 119, 212–230.

Oufi, O., Cannat, M., Horen, H., 2002. Magnetic properties of variably serpentinized abyssal peridotites. J. Geophys. Res. 107. 2095.

Plümper, O., Røyne, A., Magrasó, A., Jamtveit, B., 2012. The interface-scale mechanism of reaction-induced fracturing during serpentinization. Geology 40, 1103–1106.

Rouméjon, S., Cannat, M., 2014. Serpentinization of mantle-derived peridotites at mid-ocean ridges: mesh texture development in the context of tectonic exhumation. Geochem. Geophys. Geosyst. 15.

Rudge, J.F., Kelemen, P.B., Spiegelman, M., 2010. A simple model of reaction-induced cracking applied to serpentinization and carbonation of peridotite. Earth Planet. Sci. Lett. 291, 215–227.

Rumori, C., Mellini, M., Viti, C., 2004. Oriented, non-topotactic olivine → serpentine replacement in mesh-textured, serpentinized peridotites. Eur. J. Mineral. 16, 731–741.

Seyfried Jr, W.E., Foustoukos, D.I., Fu, Q., 2007. Redox evolution and mass transfer during serpentinization: an experimental and theoretical study at 200 °C, 500 bar with implications for ultramafic-hosted hydrothermal systems at mid-ocean ridges. Geochim. Cosmochim. Acta 71, 3872–3886.

Tivey, M.A., Dyment, J., 2010. The magnetic signature of hydrothermal systems in slow-spreading environments. In: Rona, P., Devey, C., Dyment, J., Murton, B. (Eds.), AGU Monograph 188, 43–66.

Wegner, W.W., Ernst, W.G., 1983. Experimentally determined hydration and dehydration reaction rates in the system $MgO–SiO_2–H_2O$. Am. J. Sci. 283-A, 151–180.

Wicks, F.J., Whittaker, E.J.W., 1977. Serpentine texture and serpentinization. Can. Mineral. 15, 459–488.